Nanoscale

PAPER

View Article Online
View Journal | View Issue

Cite this: *Nanoscale*, 2015, **7**, 9204

Electronic grade and flexible semiconductor film employing oriented attachment of colloidal ligand-free PbS and PbSe nanocrystals at room temperature†

G. Shiva Shanker,[a] Abhishek Swarnkar,[a] Arindom Chatterjee,[b] S. Chakraborty,[c] Manabjyoti Phukan,[a] Naziya Parveen,[a] Kanishka Biswas[b] and Angshuman Nag*[a]

Received 12th February 2015,
Accepted 4th April 2015

DOI: 10.1039/c5nr01016k

www.rsc.org/nanoscale

Electronic grade semiconductor films have been obtained *via* the sintering of solution processed PbS and PbSe nanocrystals at room temperature. Prior attempts to achieve similar films required the sintering of nanocrystals at higher temperatures (>350 °C), which inhibits the processing of such films on a flexible polymer substrate, and it is also expensive. We reduced the sintering temperature by employing two important strategies: (i) use of ligand-free nanocrystals and (ii) oriented attachment of nanocrystals. Colloidal ligand-free PbS and PbSe nanocrystals were synthesized at 70 °C with high yield (~70%). However, these nanocrystals start to agglomerate with time in formamide, and upon the removal of the solvation energy, nanocrystals undergo oriented attachment, forming larger elongated crystals. PbS and PbSe nanocrystal films made on both glass and flexible substrates at room temperature exhibit Ohmic behavior with optimum DC conductivities of 0.03 S m^{-1} and 0.08 S m^{-1}, respectively. Mild annealing of the films at 150 °C increases the conductivity values to 1.1 S m^{-1} and 137 S m^{-1} for PbS and PbSe nanocrystal films, respectively. AC impedance was measured to distinguish the contributions from grain and grain boundaries to the charge transport mechanism. Charge transport properties remain similar after the repeated bending of the film on a flexible polymer substrate. Reasonably high thermoelectric Seebeck coefficients of 600 μV K^{-1} and 335 μV K^{-1} for PbS and PbSe nanocrystal pellets, respectively, were obtained at room temperature.

1. Introduction

Solution processibility of organic materials, inorganic semiconductor (SC) nanocrystals (NCs), and molecular inorganic complexes offers easy and efficient fabrication of SC films with the potential to reduce the cost of commercial SC devices,[1–7] and also the possibility to achieve mechanically flexible devices.[8,9] Soluble organometallic compounds and hydrazinium chalcogenidometallates have been used as precursors to grow SC films in the recent past.[10,11] Films of these precursors get decomposed at an elevated temperature to form thin films of a desired inorganic SC. Typically, a large weight loss (>25%) is observed during the decomposition of precursors, generating cracks in the film. On the other hand, colloidal SC NCs are typically capped with insulating organic ligands that inhibit charge transport in the NC film.[12] Various types of surface chemistry modifications have significantly improved the charge transport of NC films, where NCs retain their crystallite size but get electronically connected.[12–16] However, the grain boundary effect still remains detrimental for charge transport. Sintering of such NC films has already been found to increase the crystallite size, and thus reduce the vexing problem of grain boundaries.

Alivisatos and co-workers demonstrated that the solution processed CdSe and CdTe nanorods could be sintered at 400 °C to form CdSe/CdTe bi-layer films for solar cell applications.[3] Jasieniak *et al.*[17] and Talapin *et al.*[18] sintered CdTe NC precursors at ~350 °C to grow CdTe films for solar cell applications. Agrawal *et al.*[19] and Korgel *et al.*[20] sintered copper–zinc–tin–sulfide (CZTS) and copper–indium–gallium–selenide (CIGS) NCs at ~500 °C. Talapin *et al.* demonstrated

[a]*Department of Chemistry, Indian Institute of Science Education and Research (IISER), Pune, 411008, India. E-mail: angshuman@iiserpune.ac.in*
[b]*New Chemistry Unit and Sheikh Saqr Laboratory, Jawaharlal Nehru Centre for Advanced Scientific Research (JNCASR), Jakkur P.O., Bangalore 560 064, India*
[c]*Centre for Advanced Materials, Indian Association for the Cultivation of Science, Kolkata 700032, India*

†Electronic supplementary information (ESI) available: Powder XRD, TEM, surface profilometry, infrared absorption, FESEM, *I vs. V* plot, ζ-potential, and PL data. See DOI: 10.1039/c5nr01016k

that the solid state reaction between inorganic NCs and their inorganic capping ligands (molecular metal chalcogenide) led to the formation of SC films with the desired composition.[21] Here, the film composed of NCs and ligands was again annealed at ~500 °C to obtain a dense SC film. Clearly, the sintering of NCs to achieve functional SC films is an active area of research, where NCs are annealed at temperatures >350 °C. However, such a high temperature annealing is not suitable to grow thin films on a flexible polymer substrate, which can be bent or twisted. The reduction of the annealing temperature below 150 °C will allow the growth of SC films on mechanically flexible and light-weight polymer substrates. In addition, the lowering of annealing/sintering temperature invariably reduces the cost associated with the film growth.

The requirement of a high annealing temperature for the sintering of NCs into a thin film suggests the requirement of higher activation energy for the process of NC fusion yielding larger crystals. Can we facilitate the fusion process of NCs at room temperature? To address this question, we employed two strategies: (i) using ligand-free NCs[22,23] and (ii) exploring the possibility of oriented attachment amongst NCs.[24–26] Bulky capping ligands on NCs hinder reactions between adjacent NCs; however, such capping ligands decompose after annealing at higher temperatures, causing a weight loss/discontinuity in the film, and therefore can also reduce the crystallite size. Our approach of using ligand-free NCs will overcome both these problems associated with the surface ligands. Yoreo *et al*. demonstrated that NCs could fuse and grow considerably more easily when two fusing NCs were oriented in a particular favorable crystallographic direction, a phenomenon known as oriented attachment.[26] Consequently, we targeted PbS and PbSe NCs because they have the tendency to undergo oriented attachment.[27–29]

Colloidal ligand-free PbS and PbSe NCs with dimensions of ~3 nm were prepared at 70 °C using a simple synthesis. Interestingly, after the addition of a non-solvent (removal of solvation energy), these NCs undergo oriented attachment to form larger NCs with an elongated shape (length of 53 nm and width of 23 nm for PbS NCs) at room temperature. Films (1–15 μm thick) were prepared at room temperature from the precipitated NCs on both flexible polyethylene terephthalate (PET) and glass substrates, which exhibit good charge transport properties. Four-probe DC conductivity, two-probe AC impedance and thermoelectric properties were measured. The best DC conductivities of PbS and PbSe NC films processed at room temperature are 0.03 S m^{-1} and 0.08 S m^{-1}, exhibiting linear voltage *vs*. current plots, and the conductivity values increased to 1.1 S m^{-1} and 137 S m^{-1}, respectively, after a mild annealing of the films at 150 °C. AC impedance shows a single semicircular Nyquist plot dominated by the grain boundary effect, which is a characteristic of polycrystalline SC films. Interestingly, the electrical properties do not change significantly after repeated bending of the films on a flexible PET substrate. The pellets of ligand-free PbS and PbSe NCs exhibit thermoelectric power factors of 0.06 μW cm^{-1} K^{-2} and 0.95 μW cm^{-1} K^{-2} at ~460 K, respectively.

2. Experimental section

2.1. Synthesis of ligand-free PbS NCs

A solution containing 10 mL formamide (FA) and 0.1 mmol (33.12 mg) $Pb(NO_3)_2$ was degassed under nitrogen atmosphere at 70 °C for 15 min in a 50 mL three necked round bottom flask. Then, aqueous solution (40–48 wt%) of $(NH_4)_2S$ (150 μL) was diluted in 1 mL FA and swiftly injected in the Pb^{2+} solution. The reaction was continued for another 15 min. The obtained NC dispersion was directly used for solution processed measurements and for solid state measurements. The NC dispersion was then precipitated by the addition of an adequate amount of acetonitrile, followed by centrifugation (5 min at 5000 rpm) and drying at room temperature under vacuum.

2.2. Synthesis of ligand-free PbSe NCs

Colloidal PbSe NCs were prepared inside a N_2 filled glove box. A solution containing 0.1 mmol $PbCl_2$ in 10 ml FA was heated to 70 °C for 15 min. In a different vial, 0.2 mmol Na_2Se was dissolved in 1 mL FA and added dropwise to the Pb^{2+} solution. Precipitation of PbSe NCs was similar to that of PbS NCs. Elemental analysis using energy-dispersive X-ray analysis (EDAX) did not show the presence of Cl in the final PbSe NCs. Consequently, we did not consider any additional surface passivation by Cl^-.[30]

A $PbCl_2$ precursor was prepared by mixing an aqueous solution of $Pb(NO_3)_2$ (0.015 mol in 10 mL water) with that of NaCl (0.030 mol in 10 mL water). The NaCl solution was added dropwise to the $Pb(NO_3)_2$ solution at room temperature with mild stirring, and the stirring was continued for 30 min. The precipitate was filtered using a Buchner funnel and washed thrice with water. The $PbCl_2$ precipitate was white in color and was characterized by powder X-ray diffraction (XRD).

2.3. Characterization

UV-visible-NIR absorption spectra were recorded using a lambda-45 UV/vis spectrometer. Steady state photoluminescence (PL) and PL decay dynamics (time correlated single photon counting (TCSPC)) were measured using FLS 980 (EDINBURGH Instruments). Powder XRD data were recorded using a Bruker D8 Advance X-ray diffractometer using Cu Kα radiation (1.54 Å). ζ-Potential and dynamic light scattering (DLS) data were obtained using a Nano-ZS90 from Malvern Instruments, U.K. Transmission electron microscopy (TEM) studies were carried out using a JEOL JEM 2100 F field emission transmission electron microscope at 200 kV. Field emission scanning electron microscopy (FESEM) and EDAX experiments were carried out using a Zeiss Ultra Plus scanning electron microscope. The thickness of the films was measured using a Veeco Dektar 150 surface profiler.

2.4. Deposition of NC film

Dried PbS NCs (100 mg) powder was ground using a mortar and pestle to make a fine homogeneous powder. *n*-Butanol (20 μL) was added dropwise to the powder and ground further

to make a thick paste. This process of adding *n*-butanol (20 μL) while grinding was repeated 15 times to obtain a homogeneous paste. The obtained NC paste was doctor-bladed onto cleaned glass as well as PET substrate. The area of the rectangular NC film was kept around 8 × 4 mm^2. However, the films with different dimensions can be made easily by just physically selecting the area of the substrate. The thickness of the film can be controlled by varying the thickness of a scotch-tape spacer, and also by adjusting the manual pressure on the glass-slide blade used during doctor blading. The film was prepared in ambient conditions. Some of the NC films were annealed at 150 °C for 30 min inside a nitrogen filled glove box. The same procedure was followed for making PbSe films. It should be noted that the NC precipitate was repeatedly washed with FA, and no trace of unwanted sodium and chlorine were detected by EDAX in the film or precipitate of these NCs.

2.5. DC and AC electrical measurements

The four probe DC resistivity measurements were performed with four co-linear individually spring loaded probes. Colloidal silver liquid was used to make contacts on the NC films. The probes were separated by a distance of 1.7 mm with a probe diameter of 1 mm. Current for all the measurements was supplied by a Model 6220/6221 Current Source and the voltage was obtained by a 2182A NANO VOLTMETER. The calculated conductivity values were obtained by passing current (I) through the outer two probes and measuring the voltage (V) across the inner two probes. The resistivity of NCs films was calculated using the following equation:[31]

$$\rho_s = \frac{V}{I} C \text{ and } \rho = \rho_s \omega$$

where ρ_s is the sheet resistance, C is the correction factor, ω is the thickness of the film and ρ is the resistivity.

AC impedance was measured in two-probe geometry using a computer enabled PARSTAT 2273 potentiostat/galvanostat along the film on both glass and PET substrates. Colloidal silver liquid was used to make contacts between the films, and two spring-loaded gold electrodes were used as probes. The distance between the probes was 1.5 mm. The AC perturbing voltage was kept at 500 mV in the frequency range of 2 MHz–100 Hz. The measured data were fitted in ZSimpWin 3.2 electrochemical impedance modeling software. We note that all the electrical measurements on films were done under ambient air.

2.6. Thermoelectric measurements

To measure the temperature dependent electrical transport, ligand-free PbS and PbSe NCs were pressed into parallelepiped shaped pellets (2 × 2 × 8 mm^3) at room temperature, using ~25 kN m^{-2} pressure. These pellets were then sintered at 500 K. The bar shaped samples had densities of ~95% relative to the bulk. Electrical conductivity (σ) and Seebeck coefficient (S) were measured simultaneously under helium atmosphere on a ULVAC RIKO ZEM3 from room temperature to 460 K. Heating-cooling cycles were repeated several times to avoid the sintering effect during the measurements.

3. Results and discussion

3.1. Colloidal ligand-free PbS NCs

Ligand-free colloidal PbS and PbSe NCs were prepared employing a simple single-step reaction. The yield of the reaction is ~70%, and does not involve any expensive organic capping ligand. Furthermore, the reaction is carried out at a low temperature (70 °C) and can be scaled up. All these aspects make our colloidal synthesis of NCs easily reproducible and cost-effective. These NCs do not exhibit very narrow size distribution, a parameter that is not critical in the present case because these NCs are only precursors for growing electronically active SC films with larger crystallite size.

The UV-vis-NIR absorption spectrum in Fig. 1a shows the lowest energy excitonic feature at 1.98 eV (626 nm) for colloidal PbS NCs dispersed in FA. The absorption feature is highly blue

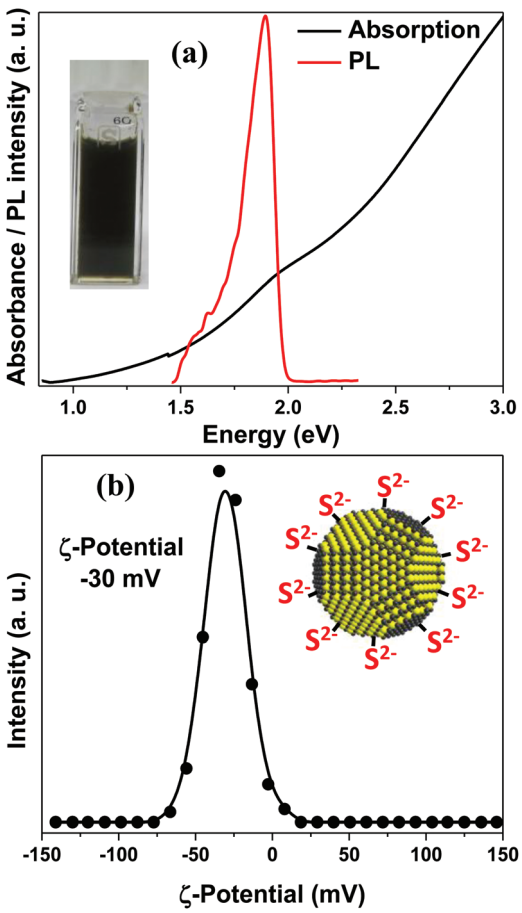

Fig. 1 (a) UV-vis-NIR absorption and PL spectra of ligand-free PbS NCs dispersed in FA. The inset shows a digital image of the colloidal dispersion of ligand-free PbS NCs in FA. (b) ζ-Potential of the ligand-free PbS NCs dispersed in FA. Inset shows a model of ligand-free PbS NCs with excess S^{2-} ($S^{\delta-}$) on the surface.

shifted compared to the bulk PbS because of the quantum confinement effect.[32] The size of colloidal PbS NCs is calculated to be 2.5 nm using the size *vs.* optical gap relation,[32] assuming that the NCs are spherical. The absorption data cannot suggest the shape of the NCs; however, they definitely suggest that the dimensions (at least one dimension) of PbS NCs are around a few nm. These PbS NCs exhibit an excitonic emission, as shown by the PL spectrum in Fig. 1a. The observation of excitonic PL suggests a lower defect density in our ligand-free PbS NCs.

The solution is colloidally stable for about a day, after which the NCs precipitate out. A digital image of the colloidal dispersion of PbS NCs in FA is shown in the inset of Fig. 1a. Fig. 1b shows the ζ-potential value of −30 mV for the as synthesized PbS NCs in FA. This negative ζ-potential establishes a negative charge on the NC surface, as schematically shown in the inset of Fig. 1b. This negative charge arises from the excess S^{2-} ($S^{\delta-}$) ions on the NC surface. These negatively charged NCs repel each other electrostatically, forming a colloidal solution in a polar solvent like FA. The counter ion NH_4^+ has a poor affinity towards the S^{2-} ions on the NC surface and remains solvated by the polar FA molecules.

3.2. Larger NCs at room temperature through oriented attachment

When the less polar acetonitrile was added to the NC dispersion in FA, the NCs precipitated out. Acetonitrile is a well-known non-solvent for precipitating/washing various types of NCs dispersed in FA.[22,33,34] However, unlike all prior cases with the NCs of CdSe, CdS, ZnS, and ZnSe,[33] our precipitated PbS NC could not be re-dispersed into pure FA solvent. More surprisingly, the XRD pattern (Fig. 2a) of these PbS NC precipitates shows sharp peaks corresponding to a mean crystallite size of ~27 nm, following the Scherrer equation.[35] The TEM image (Fig. 2b) of PbS precipitate shows elongated NCs with an average length of 53 nm and a width of 23 nm. The band gap of the PbS NC precipitate drastically decreases to 0.39 eV (Fig. S1 in ESI†), compared to that (1.98 eV) of colloidal NCs before precipitation. The obtained band gap of the PbS NC precipitate corresponds to that of the bulk PbS, confirming that the crystallite size is >18 nm, which is the value for the Bohr excitonic radius of PbS.[32] Unambiguously, the crystallite size of PbS NCs in the precipitate is about an order of magnitude larger compared to that of the colloidal (prior to the precipitation) NCs, which was observed from the UV-vis-NIR spectrum.

To understand the post-synthetic changes in the colloidal NCs, we obtained the DLS and UV-vis-NIR absorption spectra of colloidal NCs in FA after the reaction was over. The reaction mixture was isolated immediately after the injection of the S^{2-} precursor into the Pb^{2+} precursor solution in FA maintained at 70 °C. The solution was immediately cooled to room temperature, and was analysed at different time intervals. The DLS data (not shown here) do not show any particle with size greater than 5 nm after 1 min. UV-vis-NIR absorption data (Fig. 3a) show the excitonic feature of PbS NCs corresponding to the size of 2.5 nm. These results suggest that NCs are already formed but not agglomerated after 1 min. However, as the time increases, DLS data (Fig. 3b) show a systematic increase in hydrodynamic size: 14 nm after 5 min and 25 nm (along with a smaller fraction of 105 nm) after 15 min. This

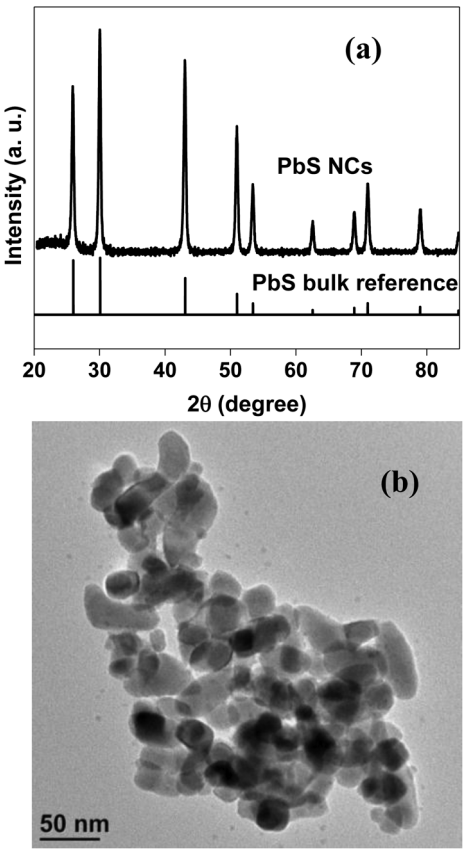

Fig. 2 (a) Powder XRD pattern and (b) TEM image of ligand-free PbS NC precipitate.

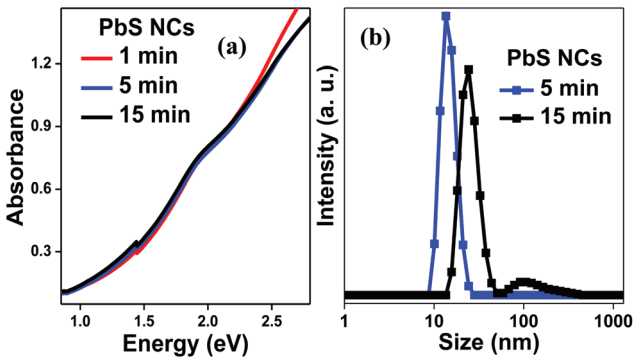

Fig. 3 Synthesis of ligand-free colloidal PbS NCs was stopped immediately after the injection of S^{2-} precursor into the Pb^{2+} solution. The solution was then cooled and maintained at room temperature. (a) UV-vis-NIR and (b) dynamic light scattering (DLS) data were measured using the same sample of PbS NCs at different times.

larger hydrodynamic radius obtained from DLS represents the size of the agglomerated structure containing many NCs, and does not necessarily mean that the size of a given NC has increased with time. In fact, the excitonic feature in both the absorption (Fig. 3a) and PL (Fig. S2 in ESI†) does not change with time, confirming that the crystallite size of a NC does not change with time; however, multiple NCs get agglomerated with time. An increase in the absorption tail at energies lower than the optical gap is also observed (Fig. 3a) with time, which again indicates the increasing tendency of the agglomeration of NCs with time. All these data suggest that the NCs undergo agglomeration with time, increasing the DLS size and absorption tail, whereas the crystallite size remains unchanged even after agglomeration; thus, the optical gap is not altered. Moreover, the colloidal solution remains stable after agglomeration, suggesting a possible solvation effect, where solvent molecules can penetrate through the porous agglomerated structure of NCs.[36] With further increase in time, agglomeration increases yielding a DLS peak >100 nm (not shown here) after many hours, eventually followed by the precipitation of NCs.

Although the NCs agglomerate in FA solvent without increasing the crystallite size, the addition of a non-solvent drastically increases the crystallite size (Fig. 2). A typical growth model,[37] including Ostwald ripening, cannot explain the sudden increase in crystal size after the addition of non-solvent. On the other hand, PbS and PbSe NCs are known to posses dipole moments along different crystallographic directions, leading to the oriented attachment of NCs.[27] The observed agglomeration of PbS NCs in FA, followed by the formation of larger NCs after the removal of FA could possibly be explained by the dipole moment of PbS NCs. Dipole moment leads to the agglomeration of NCs in FA, which has a high dielectric constant and can provide solvation energy, inhibiting the fusion of NCs. When FA molecules (solvation energy) are removed from the agglomerated structure, NCs within the agglomerated structure get fused to each other forming a larger crystallite. A similar effect of solvent polarity has been observed earlier for the fusion of SnO_2 NCs *via* oriented attachment, where the dipole–dipole attraction between NCs was found to be inversely proportional to the dielectric constant of the solvent.[38,39]

The fact that the removal of solvent molecules immediately leads to the formation of larger crystals, makes it difficult for us to collect the TEM images of smaller NCs before precipitation. Consequently, we analyzed TEM images only after the precipitation of NCs. Fig. 4a shows the fusion of multiple NCs. We concentrated on two junctions, I and II, between NCs (indicated in Fig. 4a) to investigate the possibility of oriented attachment. Fig. 4b shows a higher resolution and closer view of junctions I and II. Clearly, junction I shows the oriented attachment perpendicular to the {111} facets of the adjacent NCs, having an interplanar distance of 3.42 Å. The fast Fourier transform (FFT) pattern of Junction I in Fig. 4c shows the single crystalline nature along with diffused reciprocal spots along {111} (*i.e.*, (−1−11) and (11−1)), signifying the lattice defects/dislocations at the interface of the NCs undergoing

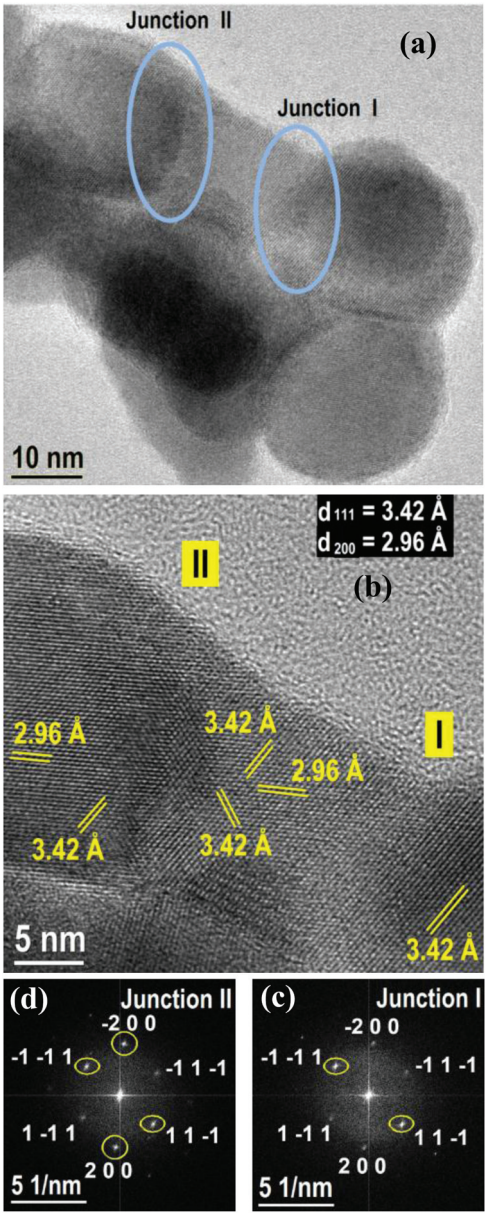

Fig. 4 (a) and (b) Show the HRTEM images of a part of the ligand-free NC precipitate. (c) and (d) Show the FFT patterns of junctions I and II, respectively. These junctions are interfaces between fusing NCs as indicated in (a) and (b).

attachment, which is in agreement with the HRTEM image showing the oriented attachment along the <111> direction of the NCs.

Junction II (Fig. 4a and b) again shows oriented attachment perpendicular to {111} facets. In addition, the {200} facets with an interplanar distance of 2.96 Å undergo lateral oriented attachment at the junction. Weller *et al.*[40] and Yoreo *et al.*[26] demonstrated similar oriented attachment both lateral (and twin-related) and perpendicular to the participating lattice planes. Fig. 4d shows the FFT pattern of junction II having diffused reciprocal spots for {111} (*i.e.*, (−1−11) and (11−1))

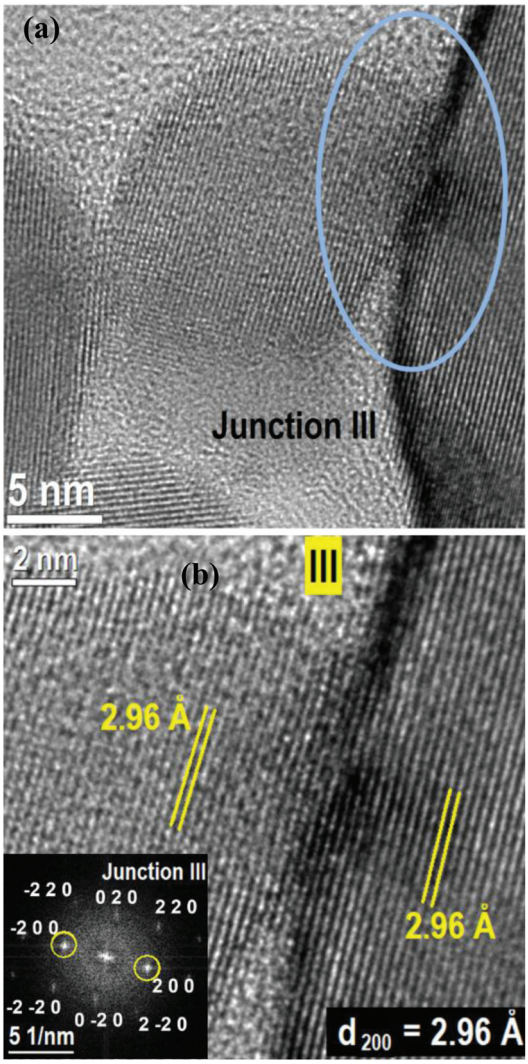

Fig. 5 (a) and (b) Show HRTEM images of another part (different from Fig. 4) of the same ligand-free NC precipitate. Inset of (b) is FFT patterns of junctions III indicated in (a) and (b).

and {200} (*i.e.*, (200) and (−200)) facets, suggesting the participation of {111} and {200} facets in the oriented attachment.

Fig. 5 shows another set of NCs undergoing oriented attachment. Here, the oriented attachment takes place perpendicular to the {200} (analogous to {100} as well) facets. The FFT pattern of junction III (inset to Fig. 5b) shows a single crystalline pattern with diffused reciprocal spots for {200} (*i.e.*, (200) and (−200)) facets, suggesting an oriented attachment along the {200} facets. We observe an oriented attachment perpendicular to both the {200} (analogous to {100}) (Fig. 5) and {111} (Fig. 4) facets. It is to be noted that the magnitude of the dipole moment is known to be high along both the <100> and <111> directions of PbS and PbSe with rock salt structure.[27] Therefore, our observation of oriented attachments along these directions again suggest the dipole–dipole interaction between NCs as a probable cause for the oriented attachment. Such oriented attachment requires easy movement of NCs, which is allowed in a colloidal dispersion, where dipole–dipole interaction is strong enough to orient adjacent NCs in a preferred crystallographic direction. Unlike colloidal dispersion, the movement of NCs gets restricted in a film. Therefore, the removal of organic ligands from the surface of PbS NCs, which were already casted into a film, yielded a film of ligand-free PbS NCs, but did not undergo oriented attachment to form larger NCs.[41] In recent times, oriented attachment has been controlled in different ways for obtaining 1D, 2D and 3D fused structures of PbS and PbSe NCs.[42,43] In our case, we have uncontrolled (both perpendicular and lateral) oriented attachment of PbS NCs giving larger elongated NCs. It should be noted that we could not capture the TEM images for smaller NCs that are present in solution because the removal of solvents leads to the formation of larger NCs.

3.3. DC and AC electrical properties of PbS NC film

Films of precipitated PbS NCs were prepared on both glass and flexible PET substrates by employing the doctor-blading technique. The inset to Fig. 6a shows a digital image of a PbS NC film on a glass substrate. The SEM image of the film in Fig. 6a shows homogenous film morphology with no unwanted pin-holes. The thickness of the film can be controlled between 1 to 15 μm (see Fig. S3 of the ESI†). The FESEM image in Fig. S4† suggests a crystallite size of ~50 nm in the film, in agreement with TEM results in Fig. 2b. Four-probe DC electrical conductivity measurements (left inset to Fig. 6b) on the PbS NC films on the glass substrate show the ohmic behavior of current (I) *vs.* voltage (V) with conductivity of 0.03 S m^{-1} for the film processed at room temperature. Upon annealing the film at 150 °C for 30 min, the conductivity increased to 1.1 S m^{-1}. The width of the XRD peaks (Fig. S5 in ESI†) decreased further after annealing, suggesting an increase in crystallite size with annealing. The obtained electrical conductivities are comparable to those of PbS films obtained by other expensive techniques that employ high temperatures and vacuum.[44] Sharp and intense XRD peaks of our NC film suggest the better crystallinity of our NCs compared to typical films made by chemical bath deposition at a low temperature.[45–47]

The electrical properties of a polycrystalline film such as our PbS NC film depend upon both inter- and intra-granular resistances. A typical DC measurement cannot differentiate between such inter- and intra-NC contributions to electrical conductivity. To obtain a better understanding about resistance and capacitance arising from both within NC (intra-granular) and grain boundaries (inter-granular), we carried out AC impedance measurements over a wide frequency range (2 MHz–100 Hz). Impedance, $\hat{Z}$ is a vector quantity and can be expressed as a complex number $\hat{Z} = Z' - iZ''$ where Z' is the real part (resistive), Z'' is the imaginary part (reactive) and $i = \sqrt{-1}$.[48] Fig. 6b shows the Nyquist plot for PbS NC films on a glass substrate, where the imaginary component, Z'' is plotted on the Y-axis with negative sign *vs.* real component, Z' on the X-axis. The Nyquist plot exhibits the shape of a single

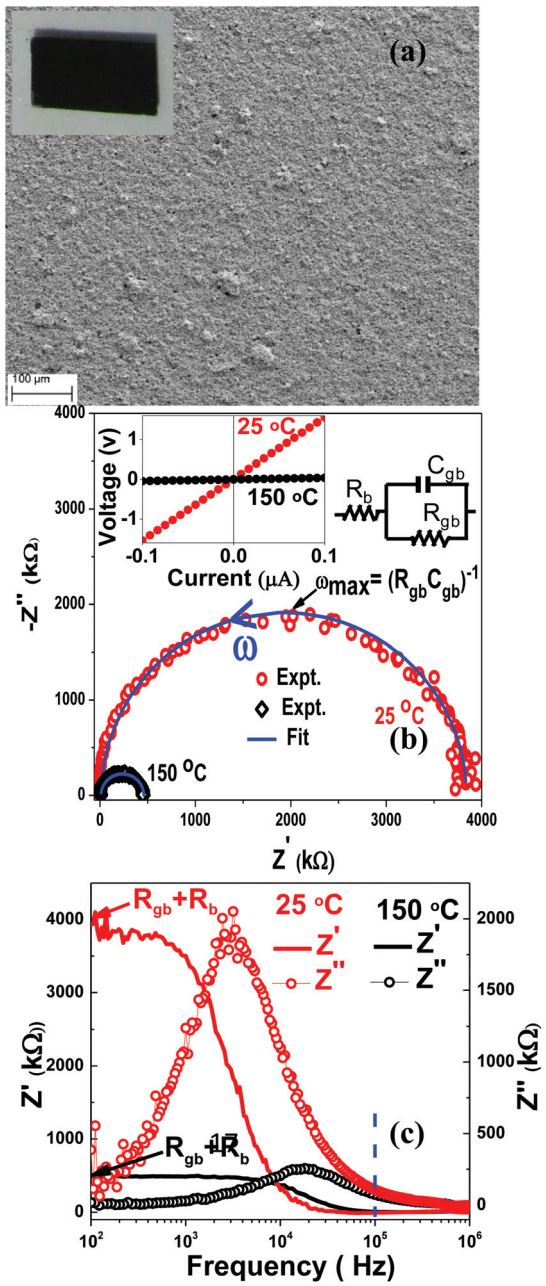

Fig. 6 (a) SEM image of a large area of PbS NC film on a glass substrate processed at room temperature. Inset shows a digital image of a typical film on glass. (b) Nyquist plots and (c) spectroscopic plot of ligand-free PbS NC films obtained from two-probe AC impedance measurements. Films were processed at 25 °C and 150 °C, but both the impedance measurements were performed at room temperature. The left inset in Fig. 6 (b) shows voltage *vs.* current plots of PbS NC films processed at 25 °C (red) and 150 °C (black). The Right inset in Fig. 6b shows a schematic electric circuit of charge conduction in PbS NC film. All the electrical measurements shown in this figure were carried out at room temperature and under ambient air.

semicircle, which is a characteristic of polycrystalline film, where the grain boundary dominates the electrical impedance.[42,49,50] The experimental data (symbols) could be fitted (blue line) well using a simple $R_b(R_{gb}C_{gb})$ electrical model (right inset to Fig. 6b),[49,50] where R_b and R_{gb} correspond to resistances due to bulk and grain boundaries, respectively, and C_{gb} is the capacitance across grain boundaries. The semicircular shape of the Nyquist plot is due to R_{gb} being parallel to C_{gb}. The radius of the semicircle would be $R_{gb}/2$ and centred at $R_{gb}/2$ if $R_b = 0$. The addition of R_b in series just shifts the curve to a higher Z' value by a small quantity of R_b. The values of R_{gb} and C_{gb} obtained from the fitting for the PbS film on the glass substrate processed at room temperature are 3.84 MΩ and 14.2 pF. The value of the capacitance matches well with the capacitance due to the grain boundary present in a typical polycrystalline film.[51] When the film was annealed at 150 °C, the radius of the semicircle decreased significantly, suggesting the decrease in R_{gb} upon annealing the film, without any considerable change in the R_b. The best fit parameter values of R_{gb} and C_{gb} for the PbS film on glass substrate annealed at 150 °C are 0.45 MΩ and 20.7 pF.

The spectroscopic plot, presented in Fig. 6c, is another way of presenting impedance as a function of frequency, where we can separate the Z' and Z'', and can analyze their dependency at different ranges of frequency. There is no considerable change in the value of Z' and Z'' at high frequencies (>10^5 Hz), indicated by the vertical blue-dashed line, whereas at lower frequencies, (<10^5 Hz) Z' and Z'' decrease significantly after annealing the film at 150 °C. The electrical responses in the high and low frequency regime typically correspond to grain and grain boundaries respectively.[42] Therefore, the observed change in charge conduction (Z' and Z'') at low frequency is attributed to the change in the characteristics of grain boundaries upon annealing the film. On the other hand, the value of the capacitance also increased after annealing the film, suggesting that the inter-granular regions were narrowed upon annealing the film.[42] Moreover, the electrical relaxation time, τ, which is the product of R_{gb} and C_{gb} and equal to $(\omega_{max})^{-1}$, was also reduced to 5.7 times after annealing the film at 150 °C, where ω_{max} is the angular frequency of maximum loss in an *RC* circuit.[42] The decrease in R_{gb} and τ along with an increase in C_{gb} after annealing the film is because of the improved electrical connectivity between adjacent NCs (grains) *via* the removal of defects from the interface of connected NCs ensuring better fusion of NCs.

We also casted similar films of PbS NCs on flexible PET substrates. The film processing was done at room temperature. The *V vs. I* plot obtained from four probe DC resistivity measurements, shown in the left-inset of Fig. 7, establishes ohmic behavior with conductivity of 0.02 S m^{-1}. The film on the PET substrate can be bent, as shown in the right-inset of Fig. 7. The film was repeatedly bent 50 times to a curvature radius of 1.1 cm, and the electrical measurements were repeated. The DC conductivity decreases to 0.015 S m^{-1} after bending the film 50 times compared to 0.02 S m^{-1} before bending. AC impedance data, as shown in Fig. 7, for the PbS NC film on PET show a semicircular Nyquist plots similar to those in Fig. 6b. The radius of the semicircle increased after bending the film repeatedly for 50 times. Both the plots,

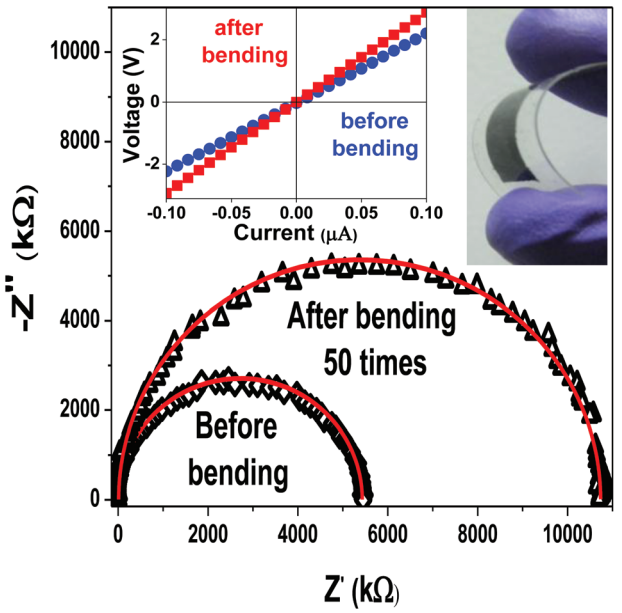

Fig. 7 Comparison of Nyquist plots (two-probe AC impedance data) of ligand-free PbS NC films on a flexible PET substrate before and after bending the film 50 times. Black symbols are experimental data and red solid lines show the fitting. The left inset shows the corresponding four-probe DC *V vs. I* plots. The right inset shows the digital image of the flexible film on PET. All the electrical measurements shown in this figure were carried out at room temperature and under ambient air.

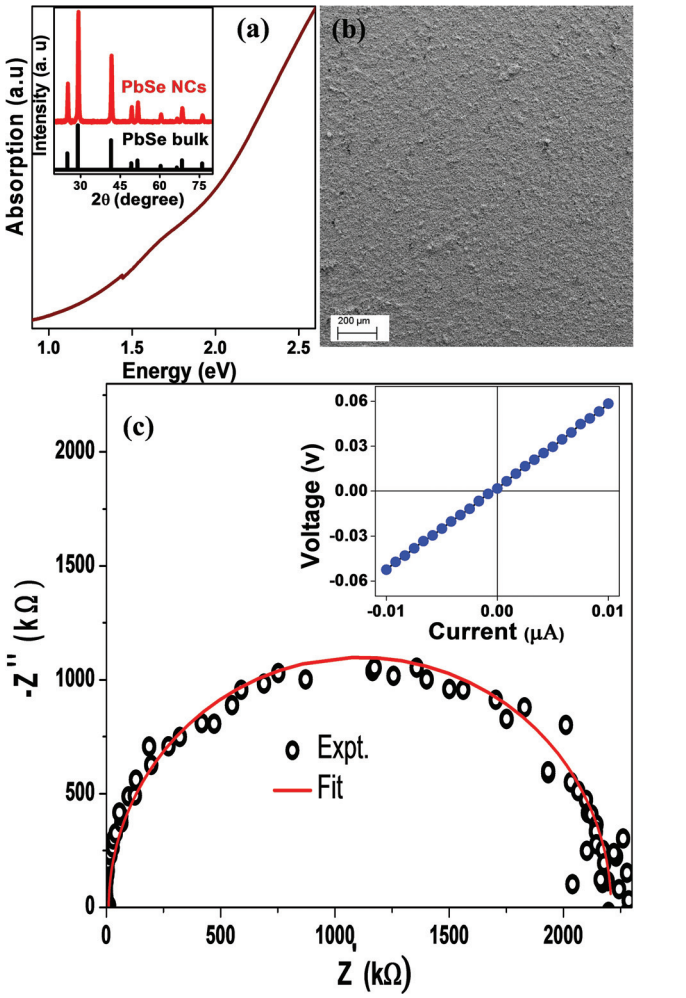

Fig. 8 (a) UV-vis-NIR absorption spectrum of ligand-free PbSe NCs dispersed in FA. Inset shows the powder XRD pattern of PbSe NCs after precipitation. (b) SEM image of a large area of PbSe NC film on glass. (c) Nyquist plot (two-probe AC impedance data) of ligand-free PbSe NC film on glass, processed at room temperature. Inset shows the corresponding DC *V vs. I* plot of the film. All the electrical measurements were carried out at room temperature and under ambient air.

before and after bending the film, can be fitted with the $R_b(R_{gb}C_{gb})$ electrical model. The best fit values of R_{gb} are 5.42 MΩ and 10.72 MΩ before and after bending the film, respectively, keeping C_{gb} largely unaltered at ~21 pF. Importantly, the film still exhibits a high electrical conductivity even after repeated bending experiments, suggesting the suitability of our PbS NC film for integration into flexible electronic devices. It should be noted that often the films made from traditional SCs generate cracks upon bending, resulting into a drastic (over many orders of magnitude) decrease in electrical conductivity.[52] The sustained electrical conductivity of the NC film after bending the film is because of the smaller size of our NC compared to the bending curvature of the film, and therefore the bending related strain is not strongly felt by NC grains and grain boundaries.

3.4. PbSe NCs

Colloidal ligand-free PbSe NCs were also prepared in a manner similar to the synthesis of ligand-free PbS NCs, but by using Na_2Se and $PbCl_2$ as sources of Se^{2-} and Pb^{2+} ions, respectively. The UV-vis-NIR absorption spectrum, presented in Fig. 8a, shows a shoulder for excitonic absorption at 1.7 eV, which corresponds to PbSe NCs with a diameter of 3.4 nm, assuming a spherical shape.[32] PbSe NCs dispersed in FA show a ζ-potential value (Fig. S6 in ESI†) of −44 mV, suggesting a negatively charged NC surface, therefore providing colloidal stability *via* electrostatic repulsion among similarly charged PbSe NCs. The NCs precipitate upon the addition of non-solvent acetonitrile, and the precipitate could not been redispersed in FA. The XRD pattern of the precipitate (inset to Fig. 8a) shows PbSe NCs with a size of ~19 nm with a rock-salt crystal structure. The TEM image in Fig. S7 of ESI† shows the fusion of small PbSe NCs, forming larger PbSe NCs. Fig. S8 in ESI† shows a band gap of 0.28 eV (4429 nm) for PbSe NC precipitate, which is similar to that of bulk PbSe. All these observations for PbSe NCs are qualitatively similar to those of PbS NCs discussed above. The removal of the solvation energy during the precipitation leads to the fusion of NCs.

Thin films of PbSe NC precipitates can be prepared on both glass and flexible PET substrates with a thickness in the range of 1–15 μm, using the doctor blading technique. Fig. 8b shows

the SEM image of a representative PbSe film on glass, showing homogeneous film morphology without any pin-holes. Fig. S9 in ESI† shows a higher magnification SEM image that exhibits elongated NCs with a diameter of ~20 nm. Four probe DC *V vs.* *I* plot for the PbSe film processed at room temperature with a conductivity of 0.08 S m^{-1} shows an ohmic behavior, as shown in the inset of Fig. 8c. After annealing the film at 150 °C, the conductivity drastically increases to 137 S m^{-1} (Fig. S10 in ESI†). The XRD pattern (Fig. S11 in ESI†) shows an increase in crystallite size *via* the narrowing of PbSe peaks after annealing at 150 °C, which explains the reason for increase in the conductivity after annealing. Two-probe AC impedance data for PbSe NC film, shown in the form of a Nyquist plot (Fig. 8c), shows a single semicircular shape with R_{gb} = 2.20 MΩ and C_{gb} = 20.4 pF. A comparison of electrical data shows that PbSe NC films are electronically more conducting compared to PbS NC films, similar to their bulk counterparts. The electrical conductivity of our PbSe NC films are comparable to the PbSe films prepared at higher temperatures using expensive methodologies.[44]

3.5. Thermoelectric measurements on NC pellets

Lead chalcogenides are well-known thermoelectric materials;[53–56] thus, we thought it would be interesting to study the thermoelectric properties of the present ligand-free PbS and PbSe NCs. For thermoelectric measurements, we used pellets of NCs after annealing at 500 K to avoid any sintering of NC during the measurements carried out at high temperatures (up to 460 K). The annealed pellets of PbS show an electrical conductivity (σ) of 2.5 S m^{-1} at room temperature, which increases to 17.6 S m^{-1} at 450 K, as shown in Fig. 9a. Similarly, the ligand-free PbSe shows a σ of 301 S m^{-1} at room temperature, which increases with increasing temperature to 699 S m^{-1} at 460 K (Fig. 9a). The increase of σ with increasing temperature reflects the semiconducting nature of the sample. Because the band gap of the PbSe (0.28 eV) is lower than that of PbS (0.39 eV), PbSe exhibits higher σ compared to PbS.

The positive sign of the Seebeck coefficient (S) indicates that PbS and PbSe are both p-type SC.[57] We speculate that the possibility of excess S or Se in our NCs might have resulted in the p-type behavior. Room temperature S is ~600 μV K^{-1}, which remains almost flat throughout the temperature range in the case of PbS (Fig. 9b). We have achieved a maximum thermoelectric power factor (σS^2) of ~0.06 μW cm^{-1} K^{-2} at 460 K in the case of PbS. In the case of PbSe, the value of S at room temperature is ~335 μV K^{-1}, which gives rise to a value of ~368 μV K^{-1} at 460 K (Fig. 9b). We achieved a maximum power factor of 0.95 μW cm^{-1} K^{-2} for PbSe at 460 K. The higher value of S in PbS compared to that in PbSe indicates that less carriers are present in the PbS than in PbSe. Reasonable thermoelectric performance obtained in the case of PbS and PbSe suggest that the NC grains are electrically well connected with each other, which is due to the organic ligand-free nature of the NCs.

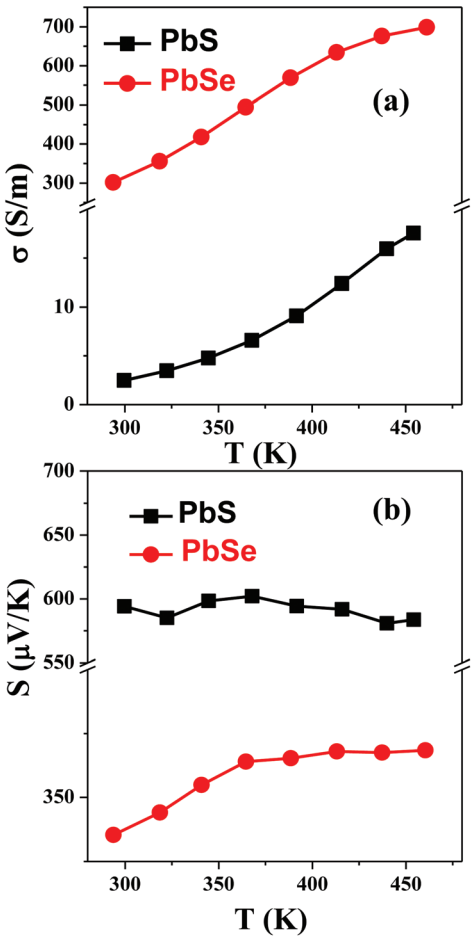

Fig. 9 Temperature dependent (a) electrical conductivity (σ) and (b) Seebeck coefficient (S) of pellets of PbS and PbSe NCs after annealing at 500 K. Data were collected under He atmosphere.

4. Conclusions

We developed a strategy to prepare electronic grade SC thin films using colloidal ligand-free PbS and PbSe NCs at room temperature. The processing at room temperature allows us to prepare films on a flexible substrate, and the charge transport properties do not deteriorate considerably with the repeated bending of the film. Therefore, the lowering of the film processing temperature allows us to obtain flexible SC films, and also it reduces the cost of film deposition. We reduced the sintering temperature of NCs by employing two strategies: (i) the preparation of ligand-free colloidal PbS and PbSe NCs and (ii) the oriented attachment of NCs. Ligand-free NCs do not have insulating organic ligands on the surface; therefore, they can provide more conducting and crack-free inorganic SC films without any further heat/chemical treatment. On the other hand, the dipole moments of PbS and PbSe NCs encourage the oriented attachment of NCs, thus reducing the activation energy of the fusion of NCs, which results in the formation of single-crystalline larger sized crystals even at room temperature. The organic-free surface of the NCs also probably support

the easier fusion of NCs. The colloidal NCs undergo oriented attachment immediately after removing the polar solvent FA during the irreversible precipitation process. DC *V vs*. *I* plots of PbS and PbSe NC films exhibit a linear ohmic behavior with electrical conductivities of 0.03 S m^{-1} and 0.08 S m^{-1}, respectively, after processing the films at room temperature. The electrical conductivities increase to 1.1 S m^{-1} and 137 S m^{-1} for PbS and PbSe, respectively, after annealing the films on glass substrates at 150 °C. AC impedance data show the dominance of grain boundaries, exhibiting single semicircular Nyquist plots. The sintered pellets of PbS and PbSe NCs exhibit thermoelectric Seebeck coefficients of 600 μV K^{-1} and 335 μV K^{-1}, respectively, at room temperature. Both the oriented attachment and organic-free colloidal NCs are generic phenomena for a variety of NC systems. Therefore, the developed strategy can possibly be extended to a variety of NC systems, including doped NCs and also heterostructured NCs, to obtain electronic grade and flexible films of functional SC. Such variation of complex compositions along with high crystallinity is difficult to achieve by employing other low-temperature film growth techniques such as chemical bath deposition.

Acknowledgements

We acknowledge Dr Shouvik Datta and Mr Amit Bhunia of IISER, Pune for AC impedance analysis. We acknowledge Prof. D. D. Sarma of Indian Institute of Science, Bangalore for useful discussion. A.N. acknowledges Science and Engineering Research Board (SERB) for Ramanujan Fellowship (SR/S2/RJN-61/2012) and fast-track research grant (SB/FT/CS-151/2012) Govt. of India. We thank Nanoscience Unit Grant (SR/NM/NS-42/2009) of DST, Govt. of India. G.S.S. acknowledges UGC, Govt. of India, for a junior research fellowship. KB acknowledges Ramanujan Fellowship, SERB and Sheikh Saqr Laboratory, JNCASR for their partial funding support.

References

1 D. B. Mitzi, L. L. Kosbar, C. E. Murray, M. Copel and A. Afzali, *Nature*, 2004, **428**, 299–303.
2 S. E. Shaheen, D. S. Ginley and G. E. Jabbour, *MRS Bull.*, 2005, **30**, 10–19.
3 I. Gur, N. A. Fromer, M. L. Geier and A. P. Alivisatos, *Science*, 2005, **310**, 462–465.
4 D. J. Milliron, D. B. Mitzi, M. Cope and C. E. Murray, *Chem. Mater.*, 2006, **18**, 587–590.
5 M. G. Panthani and B. A. Korgel, *Annu. Rev. Chem. Biomol. Eng.*, 2012, **3**, 287–311.
6 D. H. Jara, S. Yoon, K. G. Stamplecoskie and P. V. Kamat, *Chem. Mater.*, 2014, **26**, 7221–7228.
7 A. S. R. Chesman, N. W. Duffy, A. Martucci, L. D. O. Tozi, T. B. Singh and J. J. Jasieniak, *J. Mater. Chem. C*, 2014, **2**, 3247–3253.
8 D. R. Cairns and G. P. Crawford, *Proc. IEEE*, 2005, **93**, 1451–1458.
9 D. K. Kim, Y. M. Lai, T. R. Vemulkar and C. R. Kagan, *ACS Nano*, 2011, **5**, 10074–10083.
10 S. L. Castro, S. G. Bailey, R. P. Raffaelle, K. K. Banger and A. F. Hepp, *Chem. Mater.*, 2003, **15**, 3142–3147.
11 W. Liu, D. B. Mitzi, M. Yuan, A. J. Kellock, S. J. Chey and O. Gunawan, *Chem. Mater.*, 2010, **22**, 1010–1014.
12 D. V. Talapin, J. S. Lee, M. V. Kovalenko and E. V. Shevchenko, *Chem. Rev.*, 2010, **110**, 389–458.
13 W. J. Baumgardner, K. Whitham and T. Hanrath, *Nano Lett.*, 2013, **13**, 3225–3231.
14 S. J. Oh, N. E. Berry, J. H. Choi, E. A. Gaulding, H. F. Lin, T. Paik, B. T. Diroll, S. Muramoto, C. B. Murray and C. R. Kagan, *Nano Lett.*, 2014, **14**, 1559–1566.
15 S. J. Oh, Z. Q. Wang, N. E. Berry, J. H. Choi, T. S. Zhao, E. A. Gaulding, T. Paik, Y. M. Lai, C. B. Murray and C. R. Kagan, *Nano Lett.*, 2014, **14**, 6210–6216.
16 A. Nag, H. Zhang, E. Janke and D. V. Talapin, *Z. Phys. Chem.*, 2014, **229**, 85–107.
17 J. Jasieniak, B. I. MacDonald, S. E. Watkins and P. Mulvaney, *Nano Lett.*, 2011, **11**, 2856–2864.
18 M. G. Panthani, J. M. Kurley, R. W. Crisp, T. C. Dietz, T. Ezzyat, J. M. Luther and D. V. Talapin, *Nano Lett.*, 2014, **14**, 670–675.
19 Q. Guo, G. M. Ford, W. C. Yang, B. C. Walker, E. A. Stach, H. W. Hillhouse and R. Agrawal, *J. Am. Chem. Soc.*, 2010, **132**, 17384–17386.
20 T. B. Harvey, I. Mori, C. J. Stolle, T. D. Bogart, D. P. Ostrowski, M. S. Glaz, J. Du, D. R. Perniki, V. A. Akhavan, H. Kesrouani, D. A. V. Bout and B. A. Korgel, *ACS Appl. Mater. Interfaces*, 2013, **5**, 9134–9140.
21 C. Y. Jiang, J. S. Lee and D. V. Talapin, *J. Am. Chem. Soc.*, 2012, **134**, 5010–5013.
22 K. P. Kadlag, M. J. Rao and A. Nag, *J. Phys. Chem. Lett.*, 2013, **4**, 1676–1681.
23 K. P. Kadlag, P. Patil, M. J. Rao, S. Datta and A. Nag, *CrystEngComm*, 2014, **16**, 3605–3612.
24 Z. Y. Tang, N. A. Kotov and M. Giersig, *Science*, 2002, **297**, 237–240.
25 Q. Zhang, S. J. Liu and S. H. Yu, *J. Mater. Chem.*, 2009, **19**, 191–207.
26 D. S. Li, M. H. Nielsen, J. R. I. Lee, C. Frandsen, J. F. Banfield and J. J. De Yoreo, *Science*, 2012, **336**, 1014–1018.
27 K. S. Cho, D. V. Talapin, W. Gaschler and C. B. Murray, *J. Am. Chem. Soc.*, 2005, **127**, 7140–7147.
28 C. Schliehe, B. H. Juarez, M. Pelletier, S. Jander, D. Greshnykh, M. Nagel, A. Meyer, S. Foerster, A. Kornowski, C. Klinke and H. Weller, *Science*, 2010, **329**, 550–553.
29 S. Acharya, B. Das, U. Thupakula, K. Ariga, D. D. Sarma, J. Israelachvili and Y. Golan, *Nano Lett.*, 2013, **13**, 409–415.
30 J. Tang, K. W. Kemp, S. Hoogland, K. S. Jeong, H. Liu, L. Levina, M. Furukawa, X. H. Wang, R. Debnath, D. K. Cha, K. W. Chou, A. Fischer, A. Amassian,

J. B. Asbury and E. H. Sargent, *Nat. Mater.*, 2011, **10**, 765–771.
31 F. M. Smits, The Bell System Technical Journal, May 1958.
32 I. Kang and F. W. Wise, *J. Opt. Soc. Am. B*, 1997, **14**, 1632–1646.
33 A. Nag, M. V. Kovalenko, J. S. Lee, W. Y. Liu, B. Spokoyny and D. V. Talapin, *J. Am. Chem. Soc.*, 2011, **133**, 10612–10620.
34 A. Swarnkar, G. S. Shanker and A. Nag, *Chem. Commun.*, 2014, **50**, 4743–4746.
35 A. R. West, *Solid State Chemistry and its Applications*, John Wiley and Sons, Student edn, 1998, ch. 5.
36 S. Dey, B. Das, R. Voggu, A. Nag, D. D. Sarma and C. N. R. Rao, *Chem. Phys. Lett.*, 2013, **556**, 200–206.
37 R. Viswanatha, H. Amenitsch and D. D. Sarma, *J. Am. Chem. Soc.*, 2007, **129**, 4470–4475.
38 A. Y. Sinyagin, A. Belov, Z. N. Tang and N. A. Kotov, *J. Phys. Chem. B*, 2006, **110**, 7500–7507.
39 X. X. Xu, J. Zhuang and X. Wang, *J. Am. Chem. Soc.*, 2008, **130**, 12527–12535.
40 C. Pacholski, A. Kornowski and H. Weller, *Angew. Chem., Int. Ed.*, 2002, **41**, 1188.
41 H. T. Zhang, B. Hu, L. F. Sun, R. Hovden, F. W. Wise, D. A. Muller and R. D. Robinson, *Nano Lett.*, 2011, **11**, 5356–5361.
42 A. Sashchiuk, L. Amirav, M. Bashouti, M. Krueger, U. Sivan and E. Lifshitz, *Nano Lett.*, 2004, **4**, 159–165.
43 M. P. Boneschanscher, W. H. Evers, J. J. Geuchies, T. Altantzis, B. Goris, F. T. Rabouw, S. A. P. van Rossum, H. S. J. van der Zant, L. D. A. Siebbeles, G. Van Tendeloo, I. Swart, J. Hilhorst, A. V. Petukhov, S. Bals and D. Vanmaekelbergh, *Science*, 2014, **344**, 1377–1380.
44 M. Fardy, A. I. Hochbaum, J. Goldberger, M. M. Zhang and P. D. Yang, *Adv. Mater.*, 2007, **19**, 3047.
45 I. Grozdanov, M. Najdoski and S. K. Dey, *Mater. Lett.*, 1999, **38**, 28–32.
46 S. K. Sarkar, S. Kababya, S. Vega, H. Cohen, J. C. Woicik, A. I. Frenkel and G. Hodes, *Chem. Mater.*, 2007, **19**, 879–888.
47 N. B. Kotadiya, A. J. Kothari, D. Tiwari and T. K. Chaudhuri, *Appl. Phys. A: Mater. Sci. Process.*, 2012, **108**, 819–824.
48 D. C. Sinclair, *Bol. Soc, Esp. Cerám. Vidrio*, 1995, **34**, 55.
49 M. A. Ponce, M. S. Castro and C. M. Aldao, *Mater. Sci. Eng., B*, 2004, **111**, 14–19.
50 M. A. Ponce, R. Parra, R. Savu, E. Joanni, P. R. Bueno, M. Cilense, J. A. Varela and M. S. Castro, *Sens. Actuators, B*, 2009, **139**, 447–452.
51 J. T. S. Irvine, D. C. Sinclair and A. R. West, *Adv. Mater.*, 1990, **2**, 132.
52 L. B. Hu, H. S. Kim, J. Y. Lee, P. Peumans and Y. Cui, *ACS Nano*, 2010, **4**, 2955–2963.
53 K. Biswas, J. Q. He, I. D. Blum, C. I. Wu, T. P. Hogan, D. N. Seidman, V. P. Dravid and M. G. Kanatzidis, *Nature*, 2012, **489**, 414–418.
54 L. D. Zhao, S. Q. Hao, S. H. Lo, C. I. Wu, X. Y. Zhou, Y. Lee, H. Li, K. Biswas, T. P. Hogan, C. Uher, C. Wolverton, V. P. Dravid and M. G. Kanatzidis, *J. Am. Chem. Soc.*, 2013, **135**, 7364–7370.
55 Y. Z. Pei, X. Y. Shi, A. LaLonde, H. Wang, L. D. Chen and G. J. Snyder, *Nature*, 2011, **473**, 66–69.
56 J. R. Szczech, J. M. Higgins and S. Jin, *J. Mater. Chem.*, 2011, **21**, 4037–4055.
57 S. N. Guin, J. Pan, A. Bhowmik, D. Sanyal, U. V. Waghmare and K. Biswas, *J. Am. Chem. Soc.*, 2014, **136**, 12712–12720.

